Spectral signature of ice clouds in the far-infrared region: Single-scattering calculations and radiative sensitivity study

Ping Yang,[1] Martin G. Mlynczak,[2] Heli Wei,[1] David P. Kratz,[2] Bryan A. Baum,[2] Yong X. Hu,[2] Warren J. Wiscombe,[3] Andrew Heidinger,[4] and Michael I. Mishchenko[5]

[1]   We investigate the spectral signature of ice clouds in the far-infrared (far-IR) spectral region from 100 to 667 cm^{-1} (15–100 μm). Individual particle scattering properties (extinction efficiency, absorption efficiency, and the asymmetry factor of the scattering phase function) are calculated for small particles using circular cylinders and for large crystals using hexagonal columns. The scattering properties are computed for particle sizes over a size range from 1 to 10,000 μm in maximum dimension from a combination of the T-matrix method, the Lorenz-Mie theory, and an improved geometric optics method. Bulk scattering properties are derived subsequently for 30 particle size distributions, with effective particle sizes ranging from 15 to 150 μm, obtained from various field campaigns for midlatitude and tropical cirrus clouds. Furthermore, a parameterization of the bulk scattering properties is developed. The radiative properties of ice clouds and the clear-sky optical thickness computed from the line-by-line method are input to a radiative transfer model to simulate the upwelling spectral radiance in the far-IR spectral region at the research aircraft height (20 km). On the basis of the simulations, we investigate the sensitivity of far-IR spectra to ice cloud optical thickness and effective particle size. The brightness temperature difference (BTD) between 250 and 559.5 cm^{-1} is shown to be sensitive to optical thickness for optically thin clouds (visible optical thickness $\tau < 2$). At the other extreme, for optically thick ice clouds ($\tau > 8$), the BTD between 250 and 410.2 cm^{-1} is shown to be sensitive to the effective particle size up to a limit of 100 μm.   INDEX TERMS: 3359 Meteorology and Atmospheric Dynamics: Radiative processes; 3360 Meteorology and Atmospheric Dynamics: Remote sensing; 0649 Electromagnetics: Optics; KEYWORDS: far-infrared, cirrus cloud, ice crystal

1. Introduction

[2]   The radiative balance of the atmosphere is strongly influenced by the presence of cirrus clouds. Emission of infrared radiation by both water vapor and ice crystals is particularly important at long wavelengths ($\lambda > 15$ μm). However, the role that cirrus clouds play in the atmosphere, especially their radiative forcing on the global scale, is far from being well understood [*Liou*, 1986; *Stephens et al.*, 1990; *Lynch et al.*, 2002].

[3]   In recent years, significant attention has been focused on the use of high-spectral resolution interferometer mea-surements for the inference of cloud properties. These techniques primarily focus on wavelengths between 8 and 12 μm [*Ackerman et al.*, 1990; *Smith et al.*, 1993, 1998; *DeSlover et al.*, 1999; *Bantges et al.*, 1999; *Rathke et al.*, 2002; *Chung et al.*, 2000; *Kahn et al.*, 2002]. These studies indicate that data from the 8–12 μm thermal window are quite sensitive to the presence of small ice crystals when the optical thickness of the cloud is relatively small. The inference of ice cloud microphysical and optical properties is problematic for the cases with large optical thickness or large particle sizes in this spectral region.

[4]   Recent efforts explore the applicability and feasibility of far-infrared (far-IR) to microwave measurements in retrieving atmospheric parameters [*Vanek et al.*, 2001; *Mlynczak et al.*, 2002]. *Evans et al.* [1998, 1999] developed a model and provided simulations for the retrieval of cirrus cloud properties using very high-resolution submillimeter (10–150 cm^{-1}) spectral information. *Mannozzi et al.* [1999] and *Di Giuseppe and Rizzi* [1999] carried out a parameter-ization of cirrus clouds in the far-IR spectrum (10–200 cm^{-1}) based on Mie theory calculations, and found that scattering effects tend to increase the optical depth,

---

[1]Texas A&M University, Department of Atmospheric Sciences, College Station, Texas, USA.
[2]NASA Langley Research Center, Hampton, Virginia, USA.
[3]NASA Goddard Space Flight Center, Greenbelt, Maryland, USA.
[4]Office of Research and Applications, National Environmental Satellite, Data, and Information Service, National Oceanic and Atmospheric Administration, Madison, Wisconsin, USA.
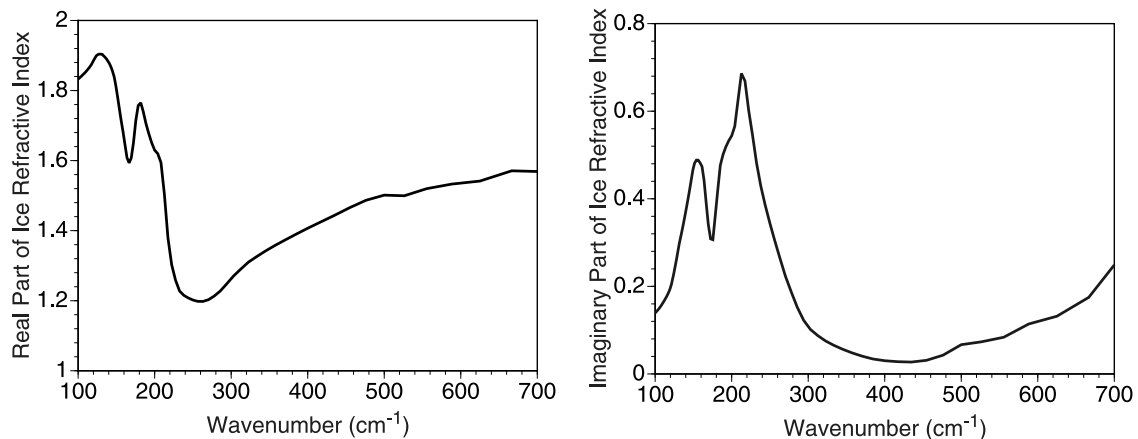[5]NASA Goddard Institute for Space Studies, New York, USA.

Figure 1. The variation of refractive index in far-IR region (data from *Warren* [1984]).

thereby reducing the upwelling longwave radiation. Our intent is to demonstrate two potential advantages that may be gained from the use of high-spectral resolution data in the far-IR spectral region. Because of the strong absorption by lower tropospheric water vapor in this spectral region, the radiation from the surface and lower atmosphere is essentially blocked [*Kratz*, 2001]. As such, the upwelling radiance from the atmosphere is fairly uniform.

[5] We investigate the sensitivity of far-IR spectra to the ice cloud optical thickness and effective particle size. The brightness temperature difference (BTD) between 250 and 559.5 cm^{-1} (hereafter referred to as BTD (250–559.5 cm^{-1})) will be used to study the sensitivity of the far-IR brightness temperature to the optical thickness for optically thin cirrus clouds (i.e., for visible optical thickness $\tau < 2$). At the other extreme, i.e., for optically thick ice clouds where $\tau > 8$, the BTD (250–410.2 cm^{-1}) is used to investigate the sensitivity of far-IR brightness temperature to the effective particle size up to 100 μm.

[6] This paper proceeds as follows. In section 2 the single-scattering properties (extinction efficiency, absorption efficiency, and the asymmetry factor of the phase function) of ice crystals are computed by using a combination of the T-matrix method, the Lorenz-Mie theory, and the geometric optics method (GOM) for spectral region 100–667 cm^{-1} (or 15–100 μm). For simplicity in light scattering computations, ice crystals are assumed to be hexagonal for large particle sizes and circular cylinders for small particle sizes. Additionally, 30 size distributions obtained from various field campaigns for midlatitude and tropical cirrus clouds are used to calculate the bulk radiative properties. In section 3 the bulk mean single-scattering properties of ice clouds are parameterized in terms of polynomial functions with respect to the effective particle size. In section 4 the sensitivity of the far-IR brightness temperature to the microphysical properties of ice clouds is investigated. The radiative properties of ice clouds and the clear-sky optical thickness computed from the line-by-line (LBL) method are input to a discrete ordinates method radiative transfer (DISORT) code [*Stamnes et al.*, 1988] to simulate the upwelling spectral radiance at a typical height (20 km) at which a research aircraft might collect data in the far-IR spectrum. The brightness temperature and their variations with respect to the microphysical properties of ice clouds at several "dirty windows" in the far-IR region are analyzed in detail. Finally, the conclusions of this study are given in section 5.

2. Single-Scattering Properties of Ice Crystals

[7] Ice clouds are almost exclusively composed of non-spherical ice crystals. Various ice crystal habits, or shapes, have been observed in cirrus clouds, including hexagonal columns and plates, bullet rosettes, and complex polycrystals and aggregates [e.g., *Heymsfield et al.*, 2002]. Although the scattering properties of ice crystals vary with crystal habit [*Evans and Stephens*, 1995], in the present study the shape of ice crystals is assumed to be a combination of hexagonal columns for large particle sizes and circular cylinders for small particle sizes. The effect of the sharp edges of the side faces of pristine ice crystals may not be important at far-IR wavelengths when particle sizes are small because of the moderate size parameters and also the strong absorption of ice in this spectral region [*Lee et al.*, 2003]. Thus the use of circular cylinders as surrogates of hexagonal columns for small pristine ice crystals does not produce substantial errors.

[8] The single-scattering properties of a particle depend on particle size, refractive index, and shape. Figure 1 shows the variation of refractive index of ice [*Warren*, 1984] in the far-IR region. On the basis of the relatively high values of the imaginary part of the refractive index, it is evident that ice crystals are strongly absorptive in the spectral region of 100–700 cm^{-1}. Additionally, the real part of the refractive index has a pronounced minimum at wave numbers in the vicinity of 250 cm^{-1}. This minimum can lead to a relatively low extinction efficiency because of a mechanism similar to the Christiansen effect [*Arnott et al.*, 1995; *Yang et al.*, 1997]. The minimum in the imaginary part of the refractive index is located around 410 cm^{-1}; the strongest scattering effect will be in this wave number region.

[9] The present calculations of single-scattering properties are performed for 168 wave numbers selected between 100 and 667 cm^{-1}. Because of the relatively weak variation of refractive index versus wave number, the scattering properties at other wave numbers that are not located at the aforementioned 168 wave numbers can be obtained by interpolation. To fully define the three-dimensional geom-
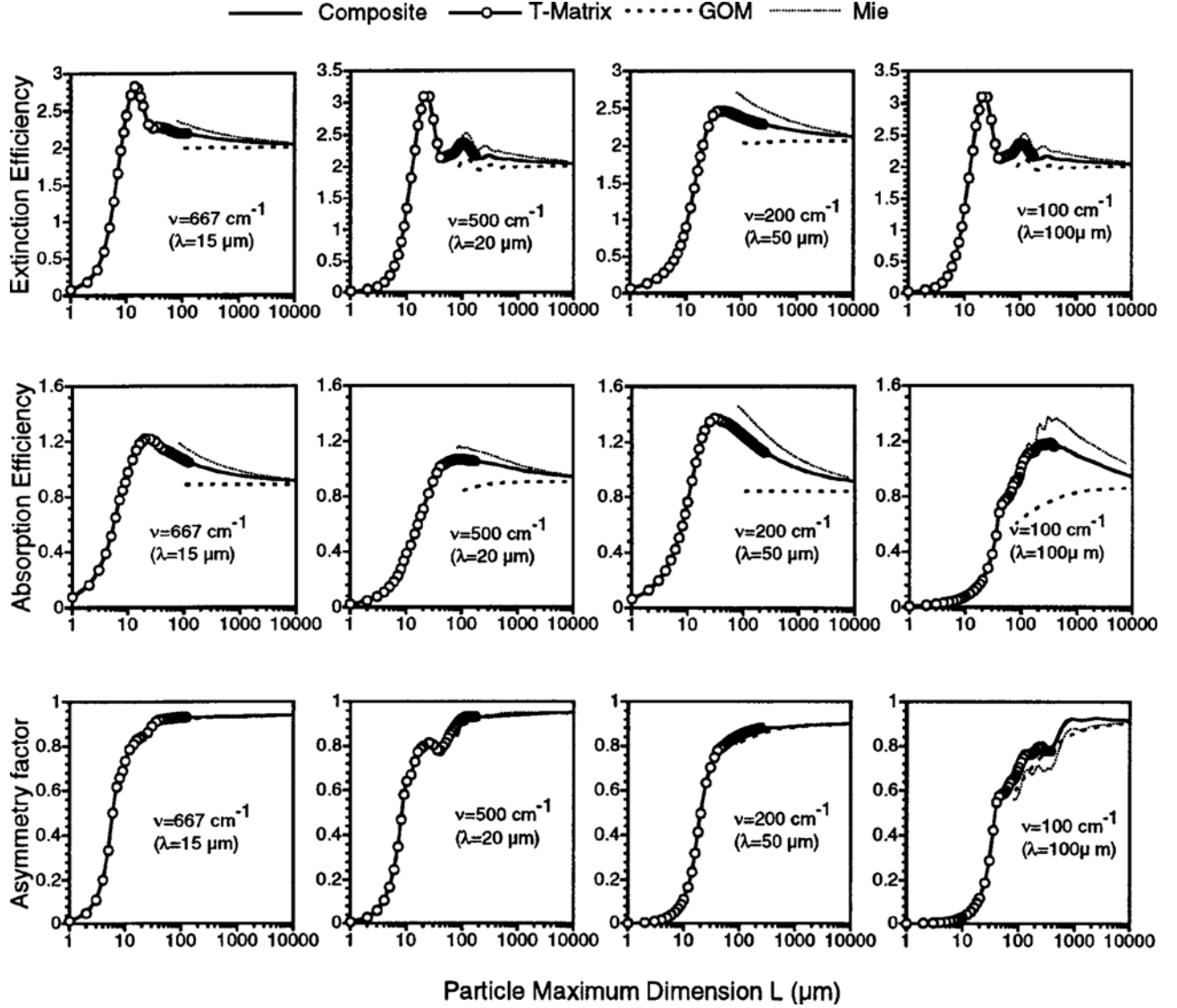
Figure 2. The extinction efficiency, absorption efficiency, and asymmetry factor of ice crystals at four wave numbers, ν = 667, 500, 200, and 100 cm^{-1} computed from T-matrix, GOM, and Mie methods. The composite results (solid) described in the text are also plotted.

etry of an ice crystal with a given size, the aspect ratio for ice crystals is defined by *Yang et al.* [2001] as $2a/L$, where L is the length of an ice crystal and a is the semiwidth of the cross section defined as:

$$a = \begin{cases} L/2, & L \leq 40\mu m \\ L/2 \exp[-0.017835(L-40)], & 40 < L < 50\mu m. \quad (1) \\ 2.958L^{1/2,} & L > 50\mu m \end{cases}$$

[10] Although a number of methods have been developed [see the recent review by *Mishchenko et al.*, 2000] for calculating the single-scattering properties of nonspherical particles, none is applicable to an arbitrary shape for a wide range of particle size parameters. The size parameter is defined as $x = \pi D_e/\lambda$, where D_e is particle effective diameter and λ is wavelength. The finite difference time domain (FDTD) [*Taflove*, 1995; *Yang and Liou*, 1995, 1996a; *Sun*

et al., 1999] and discrete dipole approximation (DDA) [*Purcell and Pennypacker*, 1973; *Draine and Flatau*, 1994] are two methods that are applicable to an arbitrary particle geometry. However, it is computationally impractical to calculate the single-scattering properties of a nonspherical particle with a size parameter larger than 20 by using the FDTD or DDA method. The T-matrix method [*Mishchenko and Travis*, 1998] can be applied to size parameters up to 200 for axisymmetrical particles. Approximate methods, such as the GOM [*Yang and Liou*, 1996b] are suitable when the particle size is much larger than the wavelength. Traditionally, an "equivalent" spherical approximation is used to compute the scattering properties of nonspherical particles, particularly at infrared wavelengths. *Fu et al.* [1998, 1999] and *Yang et al.* [2001] found that the Lorenz-Mie theory applied to equivalent spheres overestimates the scattering and absorption efficiencies in the resonance size parameter region for hexagonal columns, whereas the GOM method underestimates the efficiencies. The two methods converge for
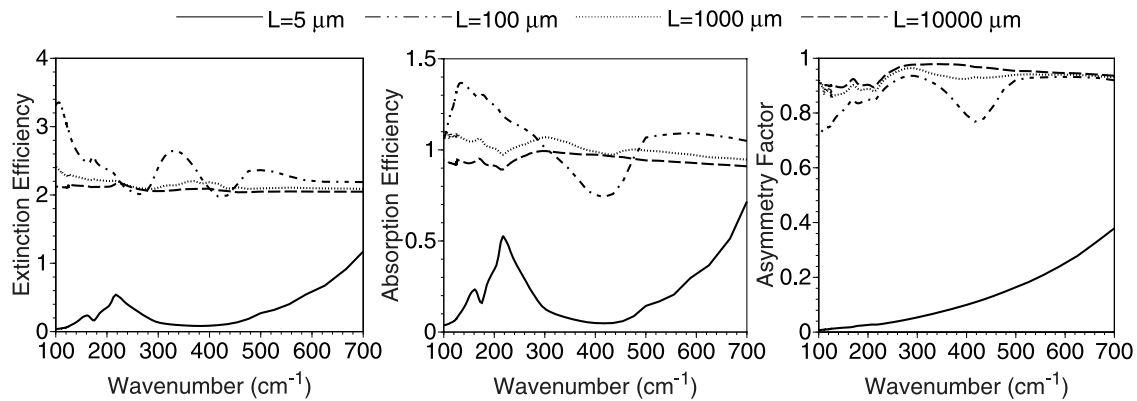
Figure 3. The variation of single-scattering properties of ice crystals as a function of wave number at four discrete ice crystal sizes (L = 5, 100, 1000, and 10,000 μm).

large particles. While we use a nonspherical model for ice crystals in light scattering computations, we note that the approach suggested by *Grenfell and Warren* [1999] presents an effective alternative, particularly for radiative flux calculations.

[11] We derive the single-scattering properties of ice crystals covering a range of sizes from 1 to 10,000 μm using the composite method suggested by *Fu et al.* [1998, 1999]. For small particles less than 120–300 μm in size, the T-matrix method is employed. For larger particles, a weighted summation of GOM and Lorenz-Mie solutions is employed to form a composite result for hexagonal ice crystals. For the weighted summation (composite result) of GOM and the Lorenz-Mie solutions, the weighting coefficients are determined in such a manner that there is no discontinuity in the transition between the T-matrix solution and the composite result. We adopt the convention by *Foot* [1988], *Francis et al.* [1994], *Mitchell and Arnott* [1994], *Fu et al.* [1998], and *Grenfell and Warren* [1999], to define the radius of an equivalent sphere as $R_e = 0.75V/A$, in which V and A are the volume and projected area of nonspherical particles, respectively.

[12] Figure 2 shows the extinction efficiency, absorption efficiency, and asymmetry factor for randomly oriented ice crystals for particle sizes ranging from 1 to 10,000 μm at wave numbers of 667, 500, 200, and 100 cm^{-1}. The composite results are provided as solid lines in the diagram. The equivalent spherical results tend to overestimate the extinction and absorption efficiencies in comparison with the nonspherical results computed by the T-matrix method, whereas GOM tends to underestimate them because of tunneling effects [e.g., *Baran et al.*, 2001] that are not considered here. The composite solution for the single-scattering properties of ice crystals, except for the asymmetry factor at a wave number of 100 cm^{-1}, varies smoothly over the range of particle sizes. The Lorenz-Mie, GOM, and the composite results converge for the case of large ice particle sizes. With the composite method, the derived single-scattering properties of ice crystals cover a wide particle size spectrum from 1 to 10,000 μm.

[13] The complex refractive indices at 667, 500, 200, and 100 cm^{-1} have the values (1.57094, 0.17489), (1.50141, 0.06688), (1.62973, 0.54398), and (1.83240, 0.13889), respectively. Because of the differences in the imaginary part

of the refractive index, the maximum in absorption efficiency at 200 cm^{-1} is higher than for the other three wave numbers. The absorption at 500 cm^{-1} is quite weak. As a result, the extinction efficiency at 500 cm^{-1} shows three resonant maxima because scattering effects dominate at this wave number.

[14] Figure 3 shows the variation of single-scattering properties as a function of wave number for four particle sizes. When the maximum dimension of an ice crystal is small (say, 5 μm), the extinction efficiency, absorption efficiency, and asymmetry factor are small. This occurs because the size parameter is small and the single-scattering properties are similar to those in the Rayleigh scattering regime. From Figures 1 and 3, it is evident that the variation of absorption efficiency with wave number for small particles depends strongly on the imaginary part of the refractive index.

[15] Figure 4 shows the contours of the extinction efficiency, absorption efficiency, and asymmetry factor of ice particles as functions of wave number and particle size. A sharp variation is evident in the transition of the values of the single-scattering properties for small particles to those for large particles. For the extinction contours, three resonant maxima are noted in the spectral region between 300 and 700 cm^{-1}, whereas only one is observed in the wave number region between 100 and 200 cm^{-1}. For the spectral region centered at 250 cm^{-1}, the extinction resonant maximum is absent and the extinction efficiency reaches its asymptotic value when the particle size is larger than approximately 100 μm. For the absorption efficiency, the transition between small and large values tends to correspond inversely to the imaginary part of the refractive index, as is evident from a comparison of Figure 1 and the second panel of Figure 4. As shown in the third panel of Figure 4, the asymmetry factor increases with particle size for a given wave number. The asymptotic value of the asymmetry factor is reached when the particle size is larger than 100 μm at a wave number of 100 cm^{-1}. At 700 cm^{-1}, the asymmetry factor reaches its asymptotic value at 30 μm.

3. Bulk Optical Properties of Cirrus Clouds and Parameterization

[16] The size distribution of ice crystals is important in the computation of the bulk, or mean, single-scattering
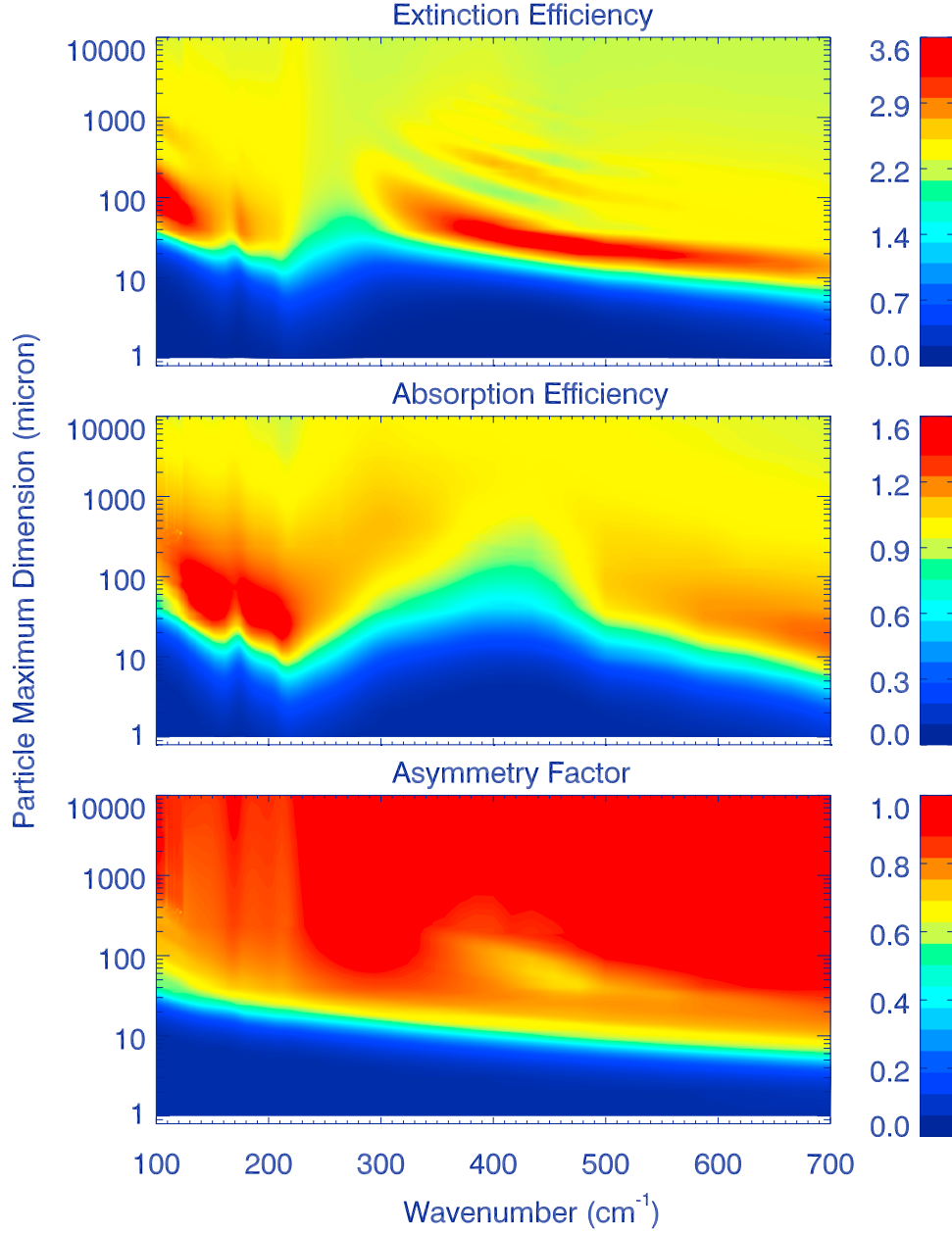
Figure 4. The extinction efficiency, absorption efficiency, and asymmetry factor of ice crystals as functions of wave number and maximum dimension.

properties of ice clouds. In this study we select the 30 size distributions from *Fu* [1996] and *Mitchell et al.* [1996]. These size distributions were measured in a variety of midlatitude and tropical cirrus clouds during several field campaigns.

[17] Following *Yang et al.* [2001], the mean extinction efficiency $\langle Q_e \rangle$, mean absorption efficiency $\langle Q_a \rangle$, mean asymmetry factor $\langle g \rangle$, and mean single-scattering albedo $\langle \omega \rangle$ are defined for cirrus clouds as follows:

$$\langle Q_e \rangle = \frac{\int_{L_{min}}^{L_{max}} Q_e(L)A(L)n(L)dL}{\int_{L_{min}}^{L_{max}} A(L)n(L)dL}, \tag{2}$$

$$\langle Q_a \rangle = \frac{\int_{L_{min}}^{L_{max}} Q_a(L)A(L)n(L)dL}{\int_{L_{min}}^{L_{max}} A(L)n(L)dL}, \tag{3}$$

$$\langle g \rangle = \frac{\int_{L_{min}}^{L_{max}} g(L)Q_s(L)A(L)n(L)dL}{\int_{L_{min}}^{L_{max}} Q_s(L)A(L)n(L)dL}, \tag{4}$$

$$\langle \omega \rangle = \frac{\int_{L_{min}}^{L_{max}} Q_s(L)A(L)n(L)dL}{\int_{L_{min}}^{L_{max}} Q_e(L)A(L)n(L)dL} = 1 - \frac{\langle Q_a \rangle}{\langle Q_e \rangle}, \tag{5}$$
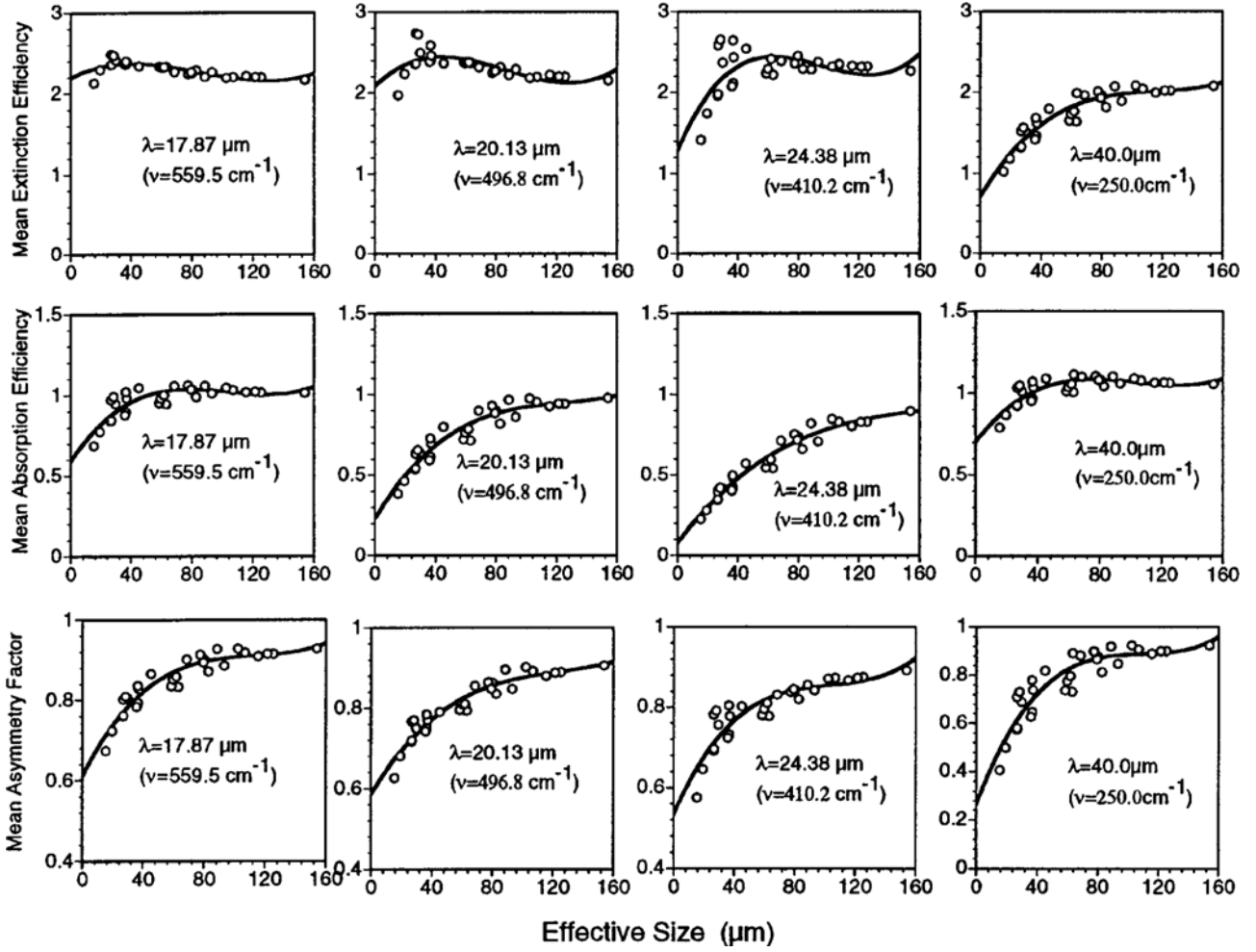
Figure 5. The mean extinction efficiency, absorption efficiency, and asymmetry factor calculated for the 30 size distributions (circle). The solid lines are curve fits in terms of a third-order polynomial function of effective particle size.

where $Q_s(L) = Q_e(L) - Q_a(L)$ is scattering efficiency, $Q_e(L)$ and $Q_a(L)$ are the extinction and absorption efficiencies calculated for individual ice crystals whose maximum dimension is denoted by L. A is particle projected area, n is the particle number density, and L_{min} and L_{max} are the minimum and maximum sizes in the size distribution.

[18] The mean single-scattering properties are functions of wave number and depend on the particle size distribution. The effective particle size provides a measure of the average size of the cloud particles for a given size distribution. There are diverse ways to define the effective particle size of nonspherical ice crystals in the literature. Following *Foot* [1988], *Francis et al.* [1994], *Fu* [1996], and *Grenfell and Warren* [1999], the effective particle size of nonspherical particles associated with a given size distribution is defined as follows:

$$D_e = \frac{3}{2} \frac{\int_{L_{min}}^{L_{max}} V(L)n(L)dL}{\int_{L_{min}}^{L_{max}} A(L)n(L)dL}, \qquad (6)$$

where V and A are the volume and projected area of an ice particle, respectively.

[19] Figure 5 shows the mean extinction efficiency, absorption efficiency, and asymmetry factor calculated for the 30 size distributions at four wave numbers. The bulk scattering properties of ice crystals are strongly dependent on the effective particle size and also sensitive to wave number. At higher wave numbers (e.g., $\nu = 559.5$ cm^{-1}), the mean extinction efficiency shows a relatively smooth variation as a function of the effective particle sizes. However, at lower wave numbers (e.g., $\nu = 250.0$ cm^{-1}), the overall pattern of the extinction efficiency indicates a monotonic increase of the efficiency with an increase in effective particle size. The absorption efficiency is much lower at 410.2 cm^{-1} than at the other three wave numbers because of the relatively small imaginary part of the ice refractive index at 410.2 cm^{-1} (see Figure 1). The mean asymmetry factor increases with an increase in effective particle size.

[20] Figure 6 shows the spectral variation of mean single-scattering properties for four particle effective particle sizes. The mean extinction efficiency tends to reach its asymptotic value at higher wave numbers ($\nu > 500$ cm^{-1}), whereas a strong dependence of the extinction efficiency on effective particle size is noted at lower wave numbers. For absorption efficiency, a pronounced sensitivity to particle size is evident
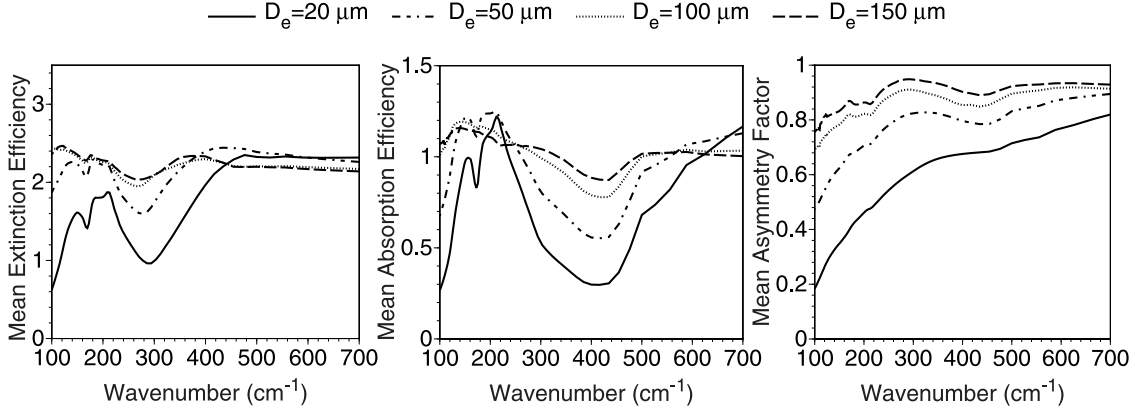
Figure 6. The variation of mean extinction efficiency, mean absorption efficiency, and mean asymmetry factor as a function of wave number for four particle sizes.

at wave numbers around 400 cm^{-1}. The mean asymmetry factor increases with both wave number and particle size. For large particles, the radiation impinging on a particle tends to be absorbed and the scattered energy is dominated by diffraction. The diffracted energy is concentrated in the forward direction, leading to a large asymmetry factor.

[21] Figure 7a shows the spectral variations of mean single-scattering albedo as a function of wave number for four effective particle sizes. Figure 7b shows the variation of the mean single-scattering albedo with effective particle size for four wave numbers. In Figure 7a, the greatest sensitivity of the mean single-scattering albedo to the effective particle size is displayed in the spectral regions between 200–300 and 350–550 cm^{-1}. Additionally, Figure 7b shows that the mean single-scattering albedo decreases with an increase in effective particle size at higher wave numbers (e.g., $\nu = 559.5$ cm^{-1}), whereas the mean single-scattering albedo increases with the effective particle size at lower wave numbers.

[22] Figure 8 shows the contours of the mean extinction efficiency, absorption efficiency, and asymmetry factor as functions of both wave number and effective particle size. The variations of extinction and absorption efficiency are related directly to the variations of both the real and imaginary parts of the refractive index. From the results shown in Figures 1 and 8, it seems that the extinction efficiency appears to be influenced primarily by the real part of the refractive index while the absorption efficiency is influenced primarily by the variation of the imaginary part of the refractive index. The values in the left lower corners of each contour plot in Figure 8 are close to zero, implying that the optically thin cirrus clouds have less effect on the radiative transfer for very small particles and lower wave numbers (longer wavelengths) in the far-IR region where the Rayleigh scattering approximation is valid.

[23] A parameterization is developed for the mean single-scattering properties in terms of third-order polynomial functions of effective particle size at each wave number as follows:

$$\langle Q_e \rangle = C_{e0} + C_{e1}D_e + C_{e2}D_e^2 + C_{e3}D_e^3, \quad (7)$$

$$\langle Q_a \rangle = C_{a0} + C_{a1}D_e + C_{a2}D_e^2 + C_{a3}D_e^3, \quad (8)$$

$$\langle g \rangle = C_{g0} + C_{g1}D_e + C_{g2}D_e^2 + C_{g3}D_e^3, \quad (9)$$

where C_{ij} ($i = e, a, g; j = 0, 1, 2, 3$) are the fitting coefficients which are functions of wavelength λ. Tables 1a–1c list these
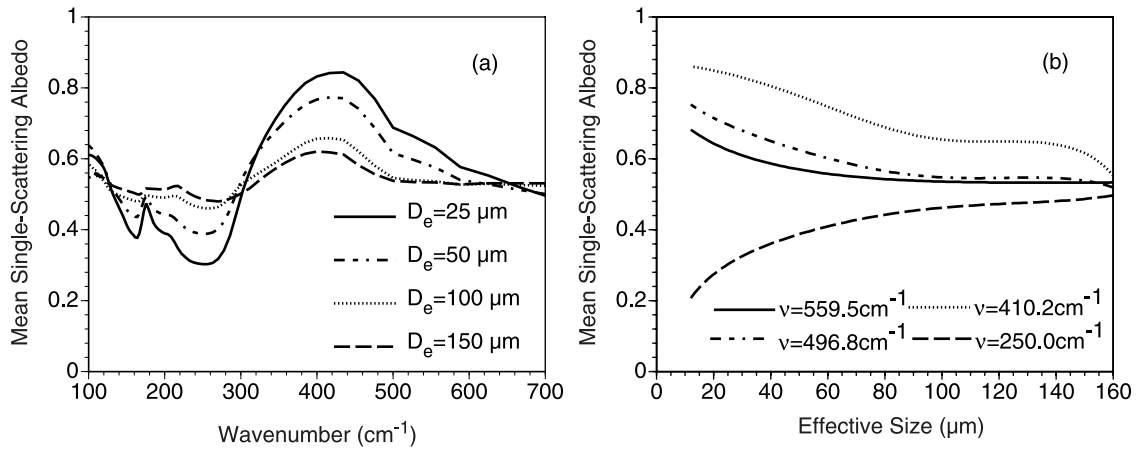

Figure 7. (a) The variation of mean single-scattering albedo as a function of wave number for four particle sizes. (b) The variation of mean single-scattering albedo as a function of particle effective particle size for four wave numbers.
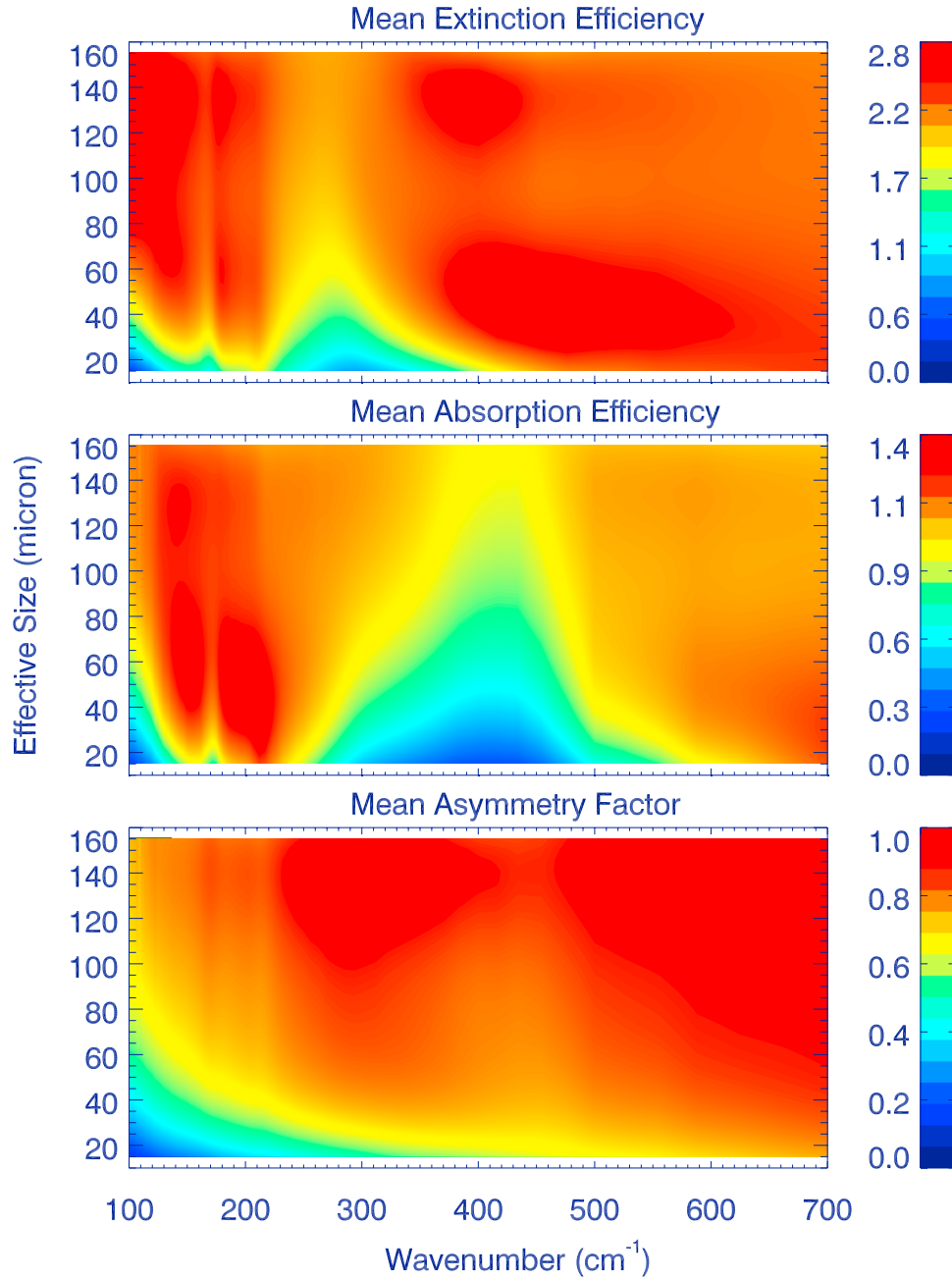
Figure 8.   Mean extinction efficiency, absorption efficiency, and asymmetry factor as functions of wave number and effective particle size.

fitting coefficients for 56 wave numbers. As an example, the parameterization results for the single-scattering properties at four wavelengths are shown in Figure 5 (solid lines).

[24] In practice, radiative transfer models often specify ice cloud properties in terms of ice water content (IWC) and effective particle size (D_e). As shown by *Yang et al.* [2001], the optical thickness of a cirrus cloud can be given as

$$\tau = \frac{3}{2} \frac{\text{IWC}}{D_e \rho_{\text{ice}}} \langle Q_e \rangle \Delta z, \tag{10}$$

where ρ_{ice} is the mass density of ice and Δz is cloud thickness. The ice water path (IWP) describes the path integration of IWC and is given by IWP = $\int_{\Delta z}$IWCdz.

[25] An alternative specification for the optical thickness of a cirrus cloud in the far-IR spectrum can be specified in terms of the visible optical thickness of the cloud by

$$\tau = \frac{\langle Q_e \rangle}{2} \tau_{\text{vis}}, \tag{11}$$

where we assume the mean extinction efficiency of ice crystals at a visible wavelength (for example, 0.55 μm) is 2. This is a reasonable assumption because of the large size parameters of typical ice particles at a visible wavelength. We will use the visible optical thickness in the subsequent analyses. Given the IWP or visible optical thickness and effective particle size of a cirrus cloud, we may obtain the

Table 1a. Fitting Coefficients in Equation (7) for the Mean Extinction Efficiencies

λ, μm	C_{e0}	C_{e1}	C_{e2}	C_{e3}
14.0	2.2700	0.0003	-2.870×10^{-5}	1.330×10^{-7}
16.0	2.2700	0.0036	-7.540×10^{-5}	3.090×10^{-7}
18.0	2.2100	0.0086	-1.420×10^{-4}	5.600×10^{-7}
20.0	2.1300	0.0137	-2.120×10^{-4}	8.230×10^{-7}
22.0	1.9500	0.0233	-3.340×10^{-4}	1.260×10^{-6}
24.0	1.5400	0.0365	-4.550×10^{-4}	1.630×10^{-6}
26.0	1.0500	0.0490	-5.600×10^{-4}	1.930×10^{-6}
28.0	0.6180	0.0577	-6.250×10^{-4}	2.110×10^{-6}
30.0	0.3060	0.0607	-6.180×10^{-4}	2.000×10^{-6}
32.0	0.1550	0.0563	-5.190×10^{-4}	1.550×10^{-6}
34.0	0.1800	0.0462	-3.740×10^{-4}	1.000×10^{-6}
36.0	0.3640	0.0372	-2.880×10^{-4}	7.630×10^{-7}
38.0	0.5480	0.0332	-2.650×10^{-4}	7.330×10^{-7}
40.0	0.7150	0.0314	-2.620×10^{-4}	7.520×10^{-7}
42.0	0.8750	0.0300	-2.620×10^{-4}	7.770×10^{-7}
44.0	1.0900	0.0283	-2.620×10^{-4}	8.120×10^{-7}
46.0	1.3400	0.0269	-2.710×10^{-4}	8.760×10^{-7}
48.0	1.3900	0.0304	-3.250×10^{-4}	1.080×10^{-6}
50.0	1.2500	0.0349	-3.710×10^{-4}	1.230×10^{-6}
52.0	1.2000	0.0376	-4.020×10^{-4}	1.330×10^{-6}
54.0	1.1500	0.0409	-4.420×10^{-4}	1.470×10^{-6}
56.0	0.9370	0.0487	-5.220×10^{-4}	1.730×10^{-6}
58.0	0.5920	0.0541	-5.460×10^{-4}	1.750×10^{-6}
60.0	0.6290	0.0488	-4.740×10^{-4}	1.480×10^{-6}
62.0	0.7770	0.0465	-4.620×10^{-4}	1.470×10^{-6}
64.0	0.8080	0.0478	-4.850×10^{-4}	1.560×10^{-6}
66.0	0.8020	0.0500	-5.160×10^{-4}	1.670×10^{-6}
68.0	0.7370	0.0536	-5.570×10^{-4}	1.810×10^{-6}
70.0	0.6370	0.0574	-5.950×10^{-4}	1.940×10^{-6}
72.0	0.5260	0.0611	-6.310×10^{-4}	2.050×10^{-6}
74.0	0.4100	0.0647	-6.640×10^{-4}	2.150×10^{-6}
76.0	0.2940	0.0681	-6.940×10^{-4}	2.230×10^{-6}
78.0	0.1570	0.0717	-7.230×10^{-4}	2.310×10^{-6}
80.0	0.0189	0.0750	-7.480×10^{-4}	2.380×10^{-6}
81.5	-0.0856	0.0771	-7.600×10^{-4}	2.400×10^{-6}
83.1	-0.1890	0.0789	-7.710×10^{-4}	2.410×10^{-6}
84.7	-0.2800	0.0803	-7.730×10^{-4}	2.400×10^{-6}
86.4	-0.3640	0.0813	-7.710×10^{-4}	2.370×10^{-6}
88.1	-0.4400	0.0822	-7.700×10^{-4}	2.330×10^{-6}
89.9	-0.5110	0.0830	-7.650×10^{-4}	2.290×10^{-6}
91.8	-0.5780	0.0836	-7.600×10^{-4}	2.240×10^{-6}
93.8	-0.6390	0.0839	-7.500×10^{-4}	2.170×10^{-6}
95.9	-0.6920	0.0839	-7.350×10^{-4}	2.090×10^{-6}
98.0	-0.7370	0.0835	-7.150×10^{-4}	1.980×10^{-6}
100.3	-0.7720	0.0826	-6.890×10^{-4}	1.850×10^{-6}
102.7	-0.7970	0.0812	-6.580×10^{-4}	1.710×10^{-6}

particle size is that ice particles have relatively stronger absorption at wavelengths between 11 and 13 μm than wavelengths between 8 and 10 μm, and the absorption depends on the ice crystal size. The upwelling radiance depends on both the optical thickness and effective particle size.

[28] There are some limitations in the use of mid-IR data for the retrieval of cloud properties. Figure 9 shows the BTD between 8.5 and 11 μm (henceforth BTD [8.5−11]) as a function of the optical thickness and effective particle size of the crystals. The BTD [8.5−11] is sensitive to small particles over a range of optical thicknesses. But, when the cloud is either optically thin or optically thick, there is little sensitivity, particularly when the effective particle size is large. The properties of optically thin or optically thick clouds are difficult to infer from mid-IR data.

[29] The inference of optically thin cirrus cloud properties using other methods such as solar reflectance algorithms is

Table 1b. Fitting Coefficients in Equation (8) for the Mean Absorption Efficiencies

λ, μm	C_{a0}	C_{a1}	C_{a2}	C_{a3}
14.0	1.2000	-0.0014	-1.170×10^{-5}	7.740×10^{-8}
16.0	0.8870	0.0085	-1.100×10^{-4}	3.920×10^{-7}
18.0	0.5810	0.0148	-1.540×10^{-4}	4.960×10^{-7}
20.0	0.3970	0.0172	-1.600×10^{-4}	4.860×10^{-7}
22.0	0.1040	0.0150	-1.030×10^{-4}	2.620×10^{-7}
24.0	0.0577	0.0135	-8.180×10^{-5}	1.870×10^{-7}
26.0	0.0638	0.0141	-8.410×10^{-5}	1.850×10^{-7}
28.0	0.1010	0.0154	-9.830×10^{-5}	2.250×10^{-7}
30.0	0.1420	0.0164	-1.120×10^{-4}	2.710×10^{-7}
32.0	0.1930	0.0168	-1.210×10^{-4}	3.060×10^{-7}
34.0	0.2740	0.0169	-1.310×10^{-4}	3.510×10^{-7}
36.0	0.4230	0.0159	-1.390×10^{-4}	4.030×10^{-7}
38.0	0.5710	0.0143	-1.370×10^{-4}	4.220×10^{-7}
40.0	0.7030	0.0124	-1.290×10^{-4}	4.150×10^{-7}
42.0	0.8240	0.0106	-1.210×10^{-4}	4.030×10^{-7}
44.0	0.9750	0.0082	-1.070×10^{-4}	3.780×10^{-7}
46.0	1.1100	0.0062	-9.920×10^{-5}	3.720×10^{-7}
48.0	1.0600	0.0090	-1.300×10^{-4}	4.770×10^{-7}
50.0	0.9470	0.0124	-1.610×10^{-4}	5.660×10^{-7}
52.0	0.8900	0.0143	-1.780×10^{-4}	6.210×10^{-7}
54.0	0.8120	0.0167	-2.010×10^{-4}	6.880×10^{-7}
56.0	0.6040	0.0213	-2.340×10^{-4}	7.660×10^{-7}
58.0	0.4620	0.0226	-2.280×10^{-4}	7.140×10^{-7}
60.0	0.5730	0.0205	-2.150×10^{-4}	6.870×10^{-7}
62.0	0.6780	0.0194	-2.150×10^{-4}	7.080×10^{-7}
64.0	0.6760	0.0202	-2.250×10^{-4}	7.460×10^{-7}
66.0	0.6420	0.0215	-2.390×10^{-4}	7.900×10^{-7}
68.0	0.5620	0.0235	-2.550×10^{-4}	8.330×10^{-7}
70.0	0.4750	0.0252	-2.660×10^{-4}	8.540×10^{-7}
72.0	0.3910	0.0267	-2.730×10^{-4}	8.600×10^{-7}
74.0	0.3120	0.0278	-2.750×10^{-4}	8.520×10^{-7}
76.0	0.2400	0.0285	-2.740×10^{-4}	8.300×10^{-7}
78.0	0.1640	0.0289	-2.660×10^{-4}	7.830×10^{-7}
80.0	0.0969	0.0287	-2.520×10^{-4}	7.180×10^{-7}
81.5	0.0525	0.0283	-2.410×10^{-4}	6.710×10^{-7}
83.1	0.0171	0.0276	-2.270×10^{-4}	6.140×10^{-7}
84.7	-0.0085	0.0268	-2.120×10^{-4}	5.550×10^{-7}
86.4	-0.0296	0.0261	-1.980×10^{-4}	4.990×10^{-7}
88.1	-0.0473	0.0253	-1.860×10^{-4}	4.510×10^{-7}
89.9	-0.0626	0.0246	-1.740×10^{-4}	4.100×10^{-7}
91.8	-0.0786	0.0241	-1.660×10^{-4}	3.750×10^{-7}
93.8	-0.0910	0.0235	-1.550×10^{-4}	3.400×10^{-7}
95.9	-0.1030	0.0229	-1.460×10^{-4}	3.050×10^{-7}
98.0	-0.1130	0.0223	-1.380×10^{-4}	2.770×10^{-7}
100.3	-0.1210	0.0218	-1.300×10^{-4}	2.530×10^{-7}
102.7	-0.1250	0.0211	-1.220×10^{-4}	2.230×10^{-7}

optical thickness, single-scattering albedo, and asymmetry factor.

[26] We now discuss the sensitivity of far-IR brightness temperatures at selected wave numbers to the microphysical and macrophysical properties of the ice clouds based on the parameterization.

4. Sensitivity of Far-IR Brightness Temperature to Ice Cloud Microphysical Properties

4.1. Retrieval Limitations Using Thermal IR Band Data (8–12 μm)

[27] Air- or spaceborne measurements of the thermal IR atmospheric spectra (8–12 μm) have been widely used to retrieve the cirrus cloud properties such as cloud height, phase, infrared optical thickness, and particle size [e.g., *Smith et al.*, 1993, 1998; *Rathke et al.*, 2002]. The basic principle for the inference of IR optical thickness and

Table 1c. Fitting Coefficients in Equation (8) for the Mean Asymmetry Factor

λ, μm	C_{g0}	C_{g1}	C_{g2}	C_{g3}
14.0	0.7360	0.0055	-5.440×10^{-5}	1.770×10^{-7}
16.0	0.6620	0.0072	-6.710×10^{-5}	2.080×10^{-7}
18.0	0.6050	0.0079	-6.910×10^{-5}	2.070×10^{-7}
20.0	0.5850	0.0077	-6.580×10^{-5}	1.950×10^{-7}
22.0	0.5770	0.0063	-4.960×10^{-5}	1.450×10^{-7}
24.0	0.5550	0.0074	-6.380×10^{-5}	1.970×10^{-7}
26.0	0.5120	0.0098	-9.310×10^{-5}	3.050×10^{-7}
28.0	0.4700	0.0117	-1.120×10^{-4}	3.620×10^{-7}
30.0	0.4280	0.0133	-1.280×10^{-4}	4.100×10^{-7}
32.0	0.3870	0.0146	-1.370×10^{-4}	4.290×10^{-7}
34.0	0.3480	0.0156	-1.440×10^{-4}	4.460×10^{-7}
36.0	0.3160	0.0162	-1.490×10^{-4}	4.600×10^{-7}
38.0	0.2880	0.0166	-1.530×10^{-4}	4.700×10^{-7}
40.0	0.2640	0.0168	-1.530×10^{-4}	4.680×10^{-7}
42.0	0.2410	0.0169	-1.530×10^{-4}	4.660×10^{-7}
44.0	0.2220	0.0168	-1.520×10^{-4}	4.600×10^{-7}
46.0	0.2060	0.0166	-1.510×10^{-4}	4.610×10^{-7}
48.0	0.1990	0.0165	-1.480×10^{-4}	4.460×10^{-7}
50.0	0.1800	0.0169	-1.490×10^{-4}	4.480×10^{-7}
52.0	0.1630	0.0170	-1.490×10^{-4}	4.460×10^{-7}
54.0	0.1480	0.0171	-1.480×10^{-4}	4.390×10^{-7}
56.0	0.1320	0.0172	-1.480×10^{-4}	4.340×10^{-7}
58.0	0.1040	0.0179	-1.520×10^{-4}	4.440×10^{-7}
60.0	0.0802	0.0183	-1.540×10^{-4}	4.450×10^{-7}
62.0	0.0681	0.0181	-1.510×10^{-4}	4.360×10^{-7}
64.0	0.0589	0.0180	-1.490×10^{-4}	4.250×10^{-7}
66.0	0.0508	0.0178	-1.460×10^{-4}	4.140×10^{-7}
68.0	0.0436	0.0176	-1.430×10^{-4}	4.030×10^{-7}
70.0	0.0353	0.0175	-1.410×10^{-4}	3.920×10^{-7}
72.0	0.0267	0.0174	-1.380×10^{-4}	3.830×10^{-7}
74.0	0.0180	0.0173	-1.360×10^{-4}	3.740×10^{-7}
76.0	0.0101	0.0172	-1.330×10^{-4}	3.630×10^{-7}
78.0	0.0017	0.0171	-1.310×10^{-4}	3.540×10^{-7}
80.0	-0.0068	0.0169	-1.280×10^{-4}	3.460×10^{-7}
81.5	-0.0123	0.0167	-1.240×10^{-4}	3.310×10^{-7}
83.1	-0.0209	0.0166	-1.230×10^{-4}	3.300×10^{-7}
84.7	-0.0303	0.0166	-1.220×10^{-4}	3.240×10^{-7}
86.4	-0.0396	0.0166	-1.210×10^{-4}	3.160×10^{-7}
88.1	-0.0489	0.0165	-1.190×10^{-4}	3.080×10^{-7}
89.9	-0.0580	0.0165	-1.180×10^{-4}	3.020×10^{-7}
91.8	-0.0684	0.0165	-1.180×10^{-4}	2.980×10^{-7}
93.8	-0.0772	0.0165	-1.160×10^{-4}	2.910×10^{-7}
95.9	-0.0869	0.0165	-1.150×10^{-4}	2.830×10^{-7}
98.0	-0.0963	0.0165	-1.140×10^{-4}	2.770×10^{-7}
100.3	-0.1050	0.0165	-1.130×10^{-4}	2.720×10^{-7}
102.7	-0.1130	0.0164	-1.110×10^{-4}	2.610×10^{-7}

by *Heidinger* [1998], and accounts for the radiatively important gases in the atmosphere (i.e., H_2O, CO_2, O_3, CO, N_2O, CH_4, etc.). We compared the simulated results based on Heidinger's model with those computed from Chou's LBL model [*Chou and Kouvaris*, 1986] and did not find substantial differences. The line parameters are taken from HITRAN-2000 [*Rothman et al.*, 1998]. The continuum absorption of water vapor and other gases within this far-IR wave number range are calculated using the CKD-2.4 model [*Tobin et al.*, 1999]. The US standard atmospheric profiles including the vertical profiles of temperature, pressure, water vapor, and ozone are used in the LBL calculations. The profiles of other trace gases are assumed to have a constant mixing ratio at each level. The atmosphere is interpolated into 100 layers below 30 km. The cloud temperature is assumed to be the same as the atmospheric temperature at that level. The surface is assumed as a blackbody (with unit emissivity 1) with a temperature of 288.15 K.

4.3. Wave Number Bands Selected for Sensitivity Study

[31] Figure 10 shows the atmospheric vertical optical thickness under clear-sky conditions from the aircraft level to the surface (0–20 km). The monochromatic optical thicknesses are degraded to 0.6 cm^{-1} spectral resolution, following *Mlynczak et al.* [2002], by a convolution with an instrumental response function that is chosen as a rectangle function with 0.6 cm^{-1} full maximum half width (FWHA). The clear-sky optical thickness from the surface to observation altitude is considerably high. Essentially, the atmosphere is opaque at far-IR wave numbers less than 400 cm^{-1}. However, the atmosphere is somewhat more transparent at some wave numbers, such as around 500 cm^{-1}, a region denoted as a "dirty window" by *Rathke et al.* [2002]. In Figure 10, specific wave numbers have been labeled as A (238.5 cm^{-1}), B (365.2 cm^{-1}), C (410.2 cm^{-1}),
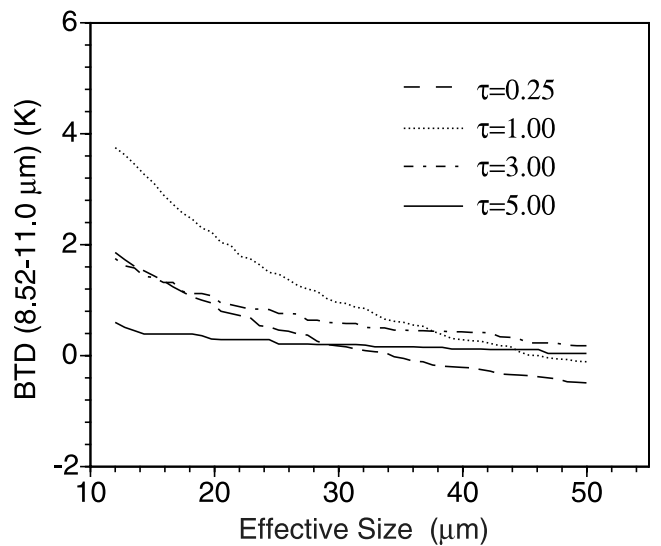
problematic, with an exception being perhaps the 1.38-μm algorithm developed by *Gao et al.* [2002]. As an important complement to these techniques, we find that the BTD of some wave numbers in the far-IR are quite sensitive to optically thin ice clouds. In the following section, we suggest a method to infer the optical thickness of thin cirrus. We also suggest a method to infer the effective particle size for optically thick ice clouds.

4.2. Far-IR Spectral Brightness Temperature Simulation

[30] To investigate the spectral radiative signature of ice clouds in the far-IR region, upwelling brightness temperatures are calculated at the cruising altitude of a research aircraft (20 km) using the DISORT code [*Stamnes et al.*, 1988] and the bulk single-scattering properties of ice clouds discussed in the previous section. The optical thicknesses of the clear-sky atmosphere at each layer are computed with a LBL radiative transfer model developed

Figure 9. The sensitivity of the brightness temperature difference (BTD) between 8.52 and 11.0 μm to effective particle size for four optical thicknesses.
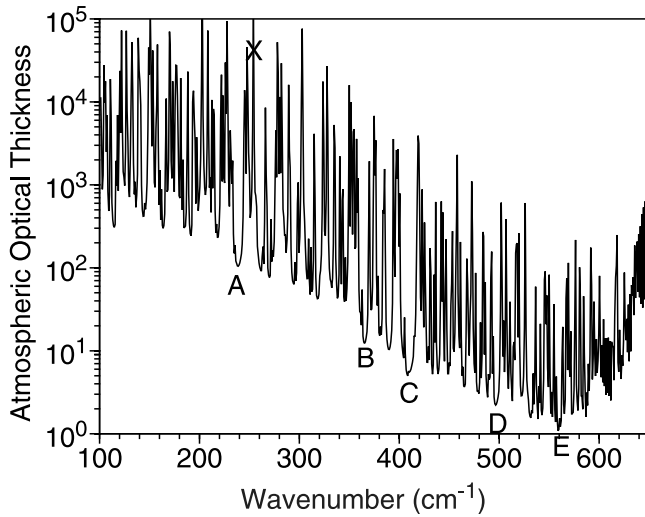
Figure 10. Atmospheric optical thickness of clear sky from the surface to 20 km altitude (U.S. standard atmosphere, the letters A–E and X indicate the channels used for retrieving the ice cloud properties in the text).

Figure 11. The far-infrared brightness spectra for a nadir view at air craft level (20 km) under clear-sky conditions as well as for cirrus clouds having different visible optical thicknesses. The clouds are located at 10 km altitude, have a 1-km geometrical thickness, and an effective particle size of $D_e = 50$ μm.

D (496.8 cm^{-1}), and E (559.5 cm^{-1}). These wave numbers are located at locations between strong water vapor absorption lines, and are more transparent than other nearby wave numbers. These labeled wave numbers are suggested as additional dirty windows. In fact, the atmosphere at such wave numbers is opaque at lower altitudes. However, at higher altitudes, the absorption is weaker and the brightness temperature at those wave numbers increases relative to other wave numbers. These wave numbers are called atmospheric dirty windows.

[32] These wave numbers, listed in Table 2, are selected for the sensitivity study of ice cloud properties not only because they are located in atmospheric dirty windows, but also because of their location in regions of strong or weak absorption in ice crystals. For example, the channels at A and E are located in regions of strong ice absorption, while channels B, C, and D are in regions of relatively weak ice absorption. The band at C has the greatest sensitivity to the scattering properties (see Figure 7) of the ice clouds. Both the scattering and absorption properties are used to infer cirrus properties. Additionally, a band is defined at 250 cm^{-1} and labeled "X" in Table 2 and Figure 10. This band is useful for inferring properties of optically thin ice clouds. The brightness temperature at this wave number is low under clear-sky conditions. The utility of this channel is to
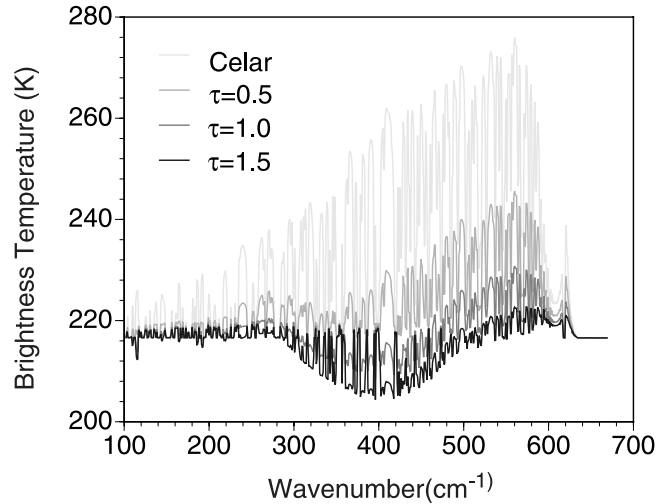
increase the sensitivity to thin cirrus clouds as will be demonstrated in the following sections.

4.4. Sensitivity of the BTD to Effective Particle Size and Optical Thickness

[33] Figure 11 shows the far-IR brightness temperature spectra for a nadir view at the research aircraft level (20 km) under clear-sky and thin cirrus cloud conditions. The calculations are performed by assuming that a cirrus cloud is located at 10 km altitude, with a 1-km geometric thickness and a effective particle size of $D_e = 50$ μm. The results demonstrate that far-IR radiation decreases if ice clouds are present. The brightness temperature decreases with increasing optical thickness.

[34] We now investigate the sensitivity of the far-IR spectal information to the microphyscial properties of the ice clouds. The study is based on the BTD between two channels: one is located at a strong water vapor absorption band (e.g., $\nu_1 = 250$ cm^{-1}), the other is at an atmospheric dirty window (e.g., $\nu_2 = 559.5$ cm^{-1}). The sensitivity to the optical thickness, particularly for optically thin cirrus clouds, increases about 20 K relative to the case for two dirty windows channels located at $\nu_1 = 238$ cm^{-1} and $\nu_2 = 559.5$ cm^{-1}.

[35] Figure 12 is the BTD derived for four visible optical thicknesses ranging from $\tau = 0.2$ to $\tau = 1.5$. The results in Figure 12 show that the brightness temperature changes nearly 29 K as optical thickness varies from 0.2 to 1.0, whereas it only increases about 9 K as the optical thickness varies from 1.0 to 1.5. The BTDs saturate at large optical thicknesses because of the strong absorption by the ice particles. The BTDs show little variation with effective particle size, varying primarily with the optical thickness. By comparison, the upwelling radiation in the thermal IR window (8–12 μm) changes with both the effective particle size and optical thickness (see the results in Figure 9 for optical thicknesses smaller than 3). We are led to conclude

Table 2. Channels Used for Retrieving Cirrus Clouds

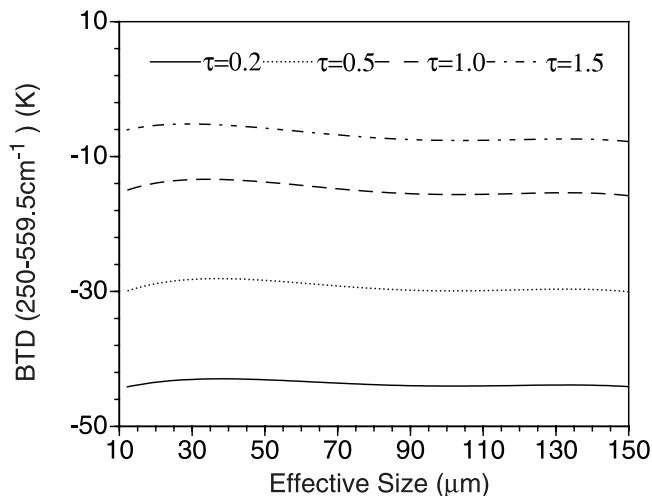|	ν, cm^{-1}	Width, cm^{-1}	Atmospheric Absorption	Scattering by Clouds (Relatively)
A	238.5	±3.0	dirty window	weak
B	365.2	±1.5	dirty window	mid strong
C	410.2	±3.0	dirty window	strongest
D	496.8	±2.0	dirty window	mid strong
E	559.5	±1.5	dirty window	weak
X	250.0	±1.0	water vapor strong absorption	weakest

Figure 12. Brightness temperature difference between two channels $\nu_1 = 250.0$ cm^{-1} and $\nu_2 = 559.5$ cm^{-1} as a function of effective particle size for four cirrus optical thicknesses.

that for ice clouds having a small optical thickness, the optical thickness may be inferred with a better accuracy using far-IR data compared to retrievals based on the mid-IR spectrum.

[36] The ensuing discussion is for a different case: that of the sensitivity of far-IR BTD to the effective particle size for ice clouds of high optical thickness. The scattering by ice particles has an influence at approximately 410 cm^{-1} and acts to decrease the radiance from the atmosphere below the clouds, resulting in a lower brightness temperature. Figure 13 shows the far-IR brightness temperature spectra for four effective particle sizes when the visible optical thickness is 10. Between 300 and 550 cm^{-1}, where scattering has an important influence, some sensivity is demonstrated for the effective particle size. From Figure 7,

the difference of single-scattering albedo between 250 and 410.2 cm^{-1} is large, and thus is dependent on the effective particle size. This feature results in the sensitivity of the BTD to the effective particle size. Figure 14 shows the variation of BTD (250–410.2 cm^{-1}) as a function of the effective particle size for three optical thicknesses. The BTD (250–410.2 cm^{-1}) values decrease with an increase of effective particle size, and are almost independent of the optical thickness when $\tau > 8$, because the differences in the single-scattering albedo between 250 and 410.2 cm^{-1} increase with the decrease of effective particle size (see Figure 7a). When the effective particle size is greater than 100 μm, the BTD reaches an asymptotic value.

[37] Figure 15 shows the variations of the BTD (250–559.5 cm^{-1}) and BTD (250–410.2 cm^{-1}) to the optical thickness for four effective particle sizes. The BTD between 250 and 559.5 cm^{-1} in Figure 15a increases with the optical thickness but displays little variation with the effective particle size when $\tau < 2$. In Figure 15b, the BTD (250–410.2 cm^{-1}) depends primarily on effective particle size when the optical thickness is greater than 5 for $D_e = 80$ μm. Furthermore, the BTD depends only on the effective particle size when optical thickness is greater than 8. When the optical thickness is within the range 2–5, the BTD is a function of both effective particle size and optical thickness.

4.5. Sensitivity to the Atmospheric Profiles

[38] Two very different atmospheric profiles are used to gain some insight as to the sensitivity of the BTDs to changes in vertical profiles of temperature and water vapor. The BTD (250–559.5 cm^{-1}) and BTD (250–410.2 cm^{-1}) values are calculated as a function of optical thickness for both a climatological tropical and subarctic winter atmosphere, with results as shown in Figure 16. Because the brightness temperature of the dirty windows for the subarctic winter atmosphere is much lower than that of tropical atmosphere, the BTD between 250 cm^{-1} and the dirty windows is higher and the sensitivity decreases for the subarctic winter atmosphere relative to a warmer tropical
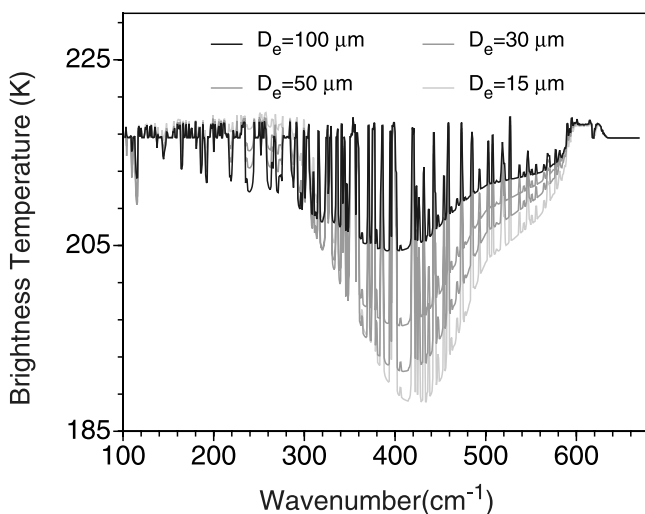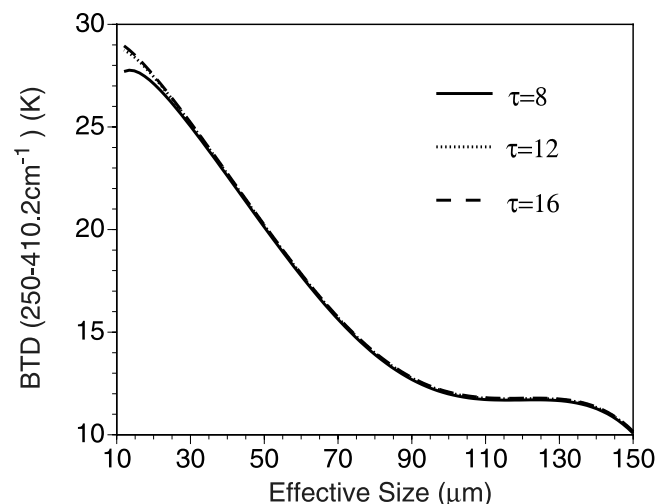

Figure 13. The far-IR brightness spectra for four effective particle sizes for optically thick ice clouds, where the visible optical thickness $\tau = 10$.

Figure 14. Brightness temperature difference between two channels $\nu_1 = 250.0$ cm^{-1} and $\nu_2 = 559.5$ cm^{-1}, for three ice cloud optical thicknesses.

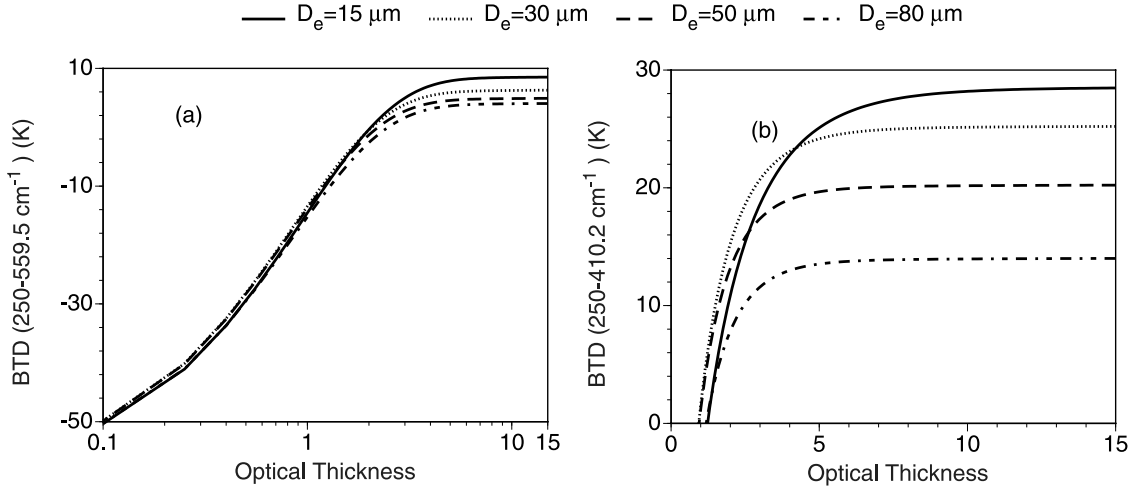**Figure 15.** The sensivity of BTD ($250-559.5$ cm^{-1}) and BTD ($250-410.2$ cm^{-1}) to optical thickness for four effective particle sizes.

atmosphere. The BTDs between 250 and 559.5 cm^{-1} in the subarctic winter atmosphere is 40.7 K higher than that of the tropical atmosphere for thin cirrus clouds when $\tau = 0.1$, and 32.8 K higher when $\tau = 3.0$. in Figure 16a. The BTDs between 250 and 410.2 cm^{-1} in the subarctic winter atmosphere is 32 K higher than that of the tropical atmosphere when the effective particle size is 15 μm, and 33.8 K higher when the effective particle size is 80 μm for an optically thick ice cloud in Figure 16b. The BTD sensivities to optical thickness for thin cirrus clouds and the effective particle size for optically thick ice clouds are shown in Table 3 for tropical, subarctic winter, and U.S. standard atmospheres. The sensitivity of BTD to optical thickness for thin cirrus clouds is only 2.0 K lower per unit optical thickness than the tropical atmosphere, with similar results for the subarctic winter atmosphere. The relative differences between the BTD values as a function of

effective particle size do not change significantly between the tropical and subarctic winter atmospheres.

4.6. Sensitivity to the Cloud Altitude

[39] The absorption of water vapor results in the atmosphere being opaque over much of the far-IR spectrum. The influence of the absorption of water vapor on the brightness temperture of ice clouds is related to the altitude of the clouds because water vapor abundance decreases with altitude.

[40] Figure 17 shows the sensivity of the BTD to the microphysical properties of ice clouds residing at four altitudes. The sensitivity to optical thickness increases with an increase in the altitude of the cloud. When the cloud altitude is lower than 4 km, there is little sensitivity of BTD to either optical thickness or particle effective particle size due to the increase in absorbtion by upper atmospheric water vapor. At cloud heights above 6 km, the sensitivity of
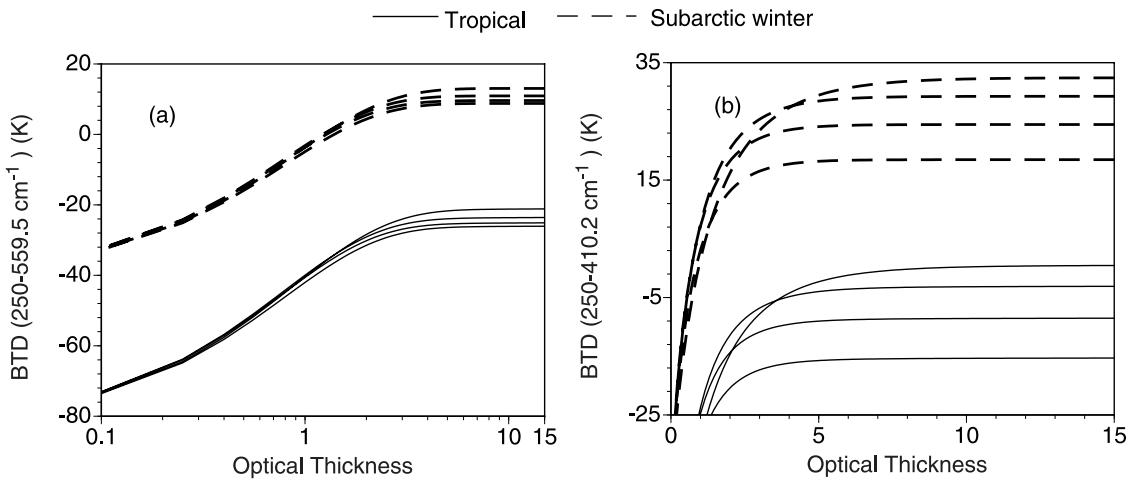

Figure 16. The BTD ($250-559.5$ cm^{-1}) and BTD ($250-410.2$ cm^{-1}) values are shown for two atmospheric models: (a) tropical standard atmosphere, and (b) subwinter standard atmposhere. The surface temperature is 300 K for the tropical model and 257.1 K for the subwinter profile. The cloud altitude is 10 km. The difference of BTD for the two atmospheric models is due primarily to the difference in surface temperature. The effective particle sizes are assumed as 15, 30, 50, and 80 μm from the top curve to the bottom for each group.

Table 3. Sensitivity of BTD (250–559.5 cm^{-1}) to Optical Thickness for Thin Cirrus Clouds and BTD (250–410.2 cm^{-1}) to the Effective Particle Size for Thick Cirrus Clouds in Tropical, Subarctic Winter, and U.S. Standard Atmosphere

	Sensitivity of BTD to Optical Thickness, K/unit Optical Thickness	Sensitivity of BTD to Effective Size, K/μm
Tropical	17.0	0.24
Subarctic winter	15.0	0.21
U.S. standard	19.0	0.22

far-IR brightness temperature to effective particle size (the slope of BTD to effective particle size) remains almost constant.

5. Summary

[41] We investigate the spectral signature of ice clouds in the far-IR spectral region from 100 to 667 cm^{-1} (15–100 μm). Individual particle scattering properties (extinction efficiency, absorption efficiency, and the asymmetry factor of the scattering phase function) are calculated for a combination of hexagonal columns (large particles) and circular cylinders (small particles). Single-scattering properties are derived for particles having maximum dimensions from 1 to 10,000 μm using a combination of the T-matrix method, the Lorenz-Mie theory, and an improved GOM. Bulk scattering properties are derived subsequently for 30 particle size distributions obtained from various field campaigns for midlatitude and tropical cirrus clouds. These distributions have effective particle sizes ranging from 15 to 150 μm. On the basis of the bulk scattering properties derived for the various size distributions, a parameterization of the bulk scattering properties is developed.

[42] The sensitivity of far-IR brightness temperature to the microphysical properties of ice clouds was investigated using a LBL radiative transfer model and the DISORT computational program. The brightness temperature and its sensitivity to the microphysical properties of ice clouds

in several dirty windows in far-IR region are discussed. The BTD between two channels (250 and 559.5 cm^{-1}) is used to investigate the sensitivity to the optical thickness for thin cirrus clouds. One channel is located in a strong absorption band sensitive to both water vapor and ice clouds. The other band is located at an atmospheric dirty window that is also sensitive to the presence of ice clouds. The BTD (250–559.5 cm^{-1}) shows some sensitivity to optical thickness when the cloud visible optical thickness is less than 2. The sensitivity is much larger than that of thermal IR window method, and is independent of the effective particle size.

[43] Under conditions when the cloud visible optical thickness is extremely high, greater than 8, the BTD between another two channels (250 and 410.2 cm^{-1}) shows a potential sensitivity to the effective particle size. One channel is located at a strong absorption band that is sensitive to the presence of both water vapor and ice particles; the other channel is located in an atmospheric dirty window that displays very low absorption but strong scattering due to the ice particles. For larger optical thicknesses, the strong scattering properties result in a much lower brightness temperature in the strong scattering channel than that located at a strong absorption band. We find that the BTD between these two channels is sensitive to the effective particle size and is independent of optical thickness. The sensitivity of BTD to optical thickness decreases with altitude. The sensitivity to effective particle size does not change significantly with the atmospheric profiles or for clouds at altitudes above 6 km.

[44] The present work provides some insight as to the potential utility of inferring ice cloud optical thickness and effective particle size from far-IR spectra. The analysis of far-IR spectra displays some sensitivity to the properties of ice clouds in regimes that complement analyses of mid-IR spectra. However, for these far-IR BTD analyses to be used in some operational sense, additional information is required such as the atmospheric temperature profile, water vapor profile, the cloud altitude, and the cloud temperature.
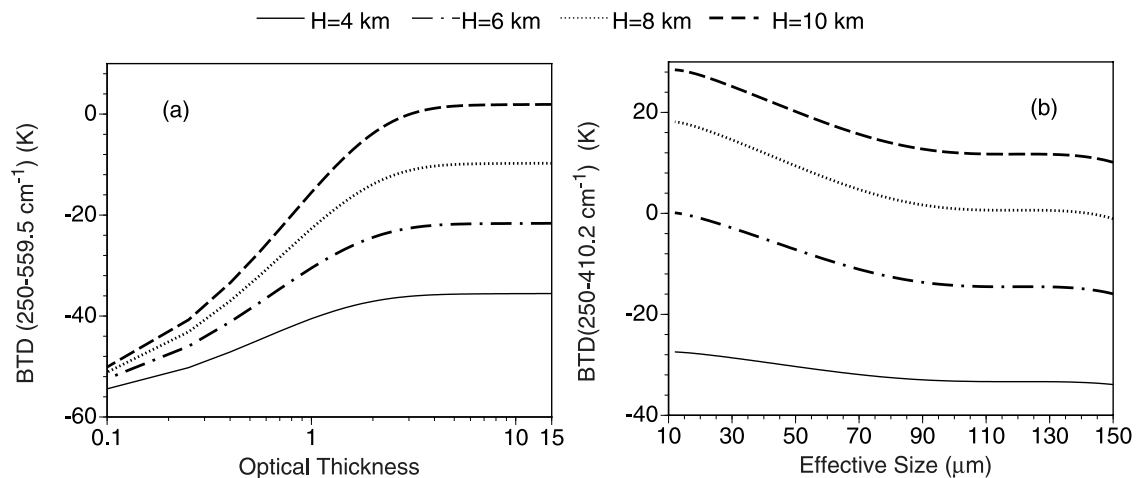

Figure 17. The sensitivity of BTD (250–559.5 cm^{-1}) and BTD (250–410.2 cm^{-1}) values to the optical thickness and effective particle size of ice crystals when cirrus clouds are located at four altitudes (H = 4, 6, 8, and 10 km). (a) The BTD (250–559.5 cm^{-1}) as a function of ice cloud visible optical thickness. The particle effective particle size is fixed at 50 μm. (b) The BTD (250–410.2 cm^{-1}) as a function of ice cloud effective particle size. The visible optical thickness is fixed at 10.

References

Ackerman, S. A., W. L. Smith, J. D. Spinhirne, and H. E. Revercomb, The 27–28 October 1986 far-IRE IFO cirrus case study: Spectral properties of cirrus clouds in the 8–12 µm window, *Mon. Weather Rev.*, 118, 2377–2388, 1990.

Arnott, W. P., Y. Y. Dong, and J. Hallett, Extinction efficiency in the infrared (2–18 µm) of laboratory ice clouds: Observations of scattering minima in the Christiansen bands of ice, *Appl. Opt.*, 34, 541–551, 1995.

Bantges, R. J., J. E. Russell, and J. D. Haigh, Cirrus cloud top-of-atmosphere radiance spectra in the thermal infrared, *J. Quant. Spectrosc. Radiat. Transfer*, 63, 487–498, 1999.

Baran, A. J., P. Yang, and S. Havemann, Calculation of the single-scattering properties of randomly oriented hexagonal ice columns: A comparison of the T-matrix and the finite-difference time-domain methods, *Appl. Opt.*, 40, 4376–4386, 2001.

Chou, M.-D., and L. Kouvaris, Monochromatic calculations of atmospheric radiative transfer due to molecular line absorption, *J. Geophys. Res.*, 91, 4047–4055, 1986.

Chung, S., S. Ackerman, P. F. Van Delst, and W. P. Menzel, Model calculations and interferometer measurements of ice-cloud characteristics, *J. Appl. Meteorol.*, 39, 634–644, 2000.

DeSlover, D. H., W. L. Smith, P. K. Piironen, and E. W. Eloranta, A methodology for measuring cirrus cloud visible-to-infrared spectral optical thickness ratios, *J. Atmos. Oceanic Technol.*, 16, 251–262, 1999.

Di Giuseppe, F., and R. Rizzi, Far infrared scattering effects in cloudy sky, *Phys. Chem. Earth*, 24, 243–247, 1999.

Draine, B. T., and P. J. Flatau, Discrete-dipole approximation for scattering calculations, *J. Opt. Soc. Am. A. Opt. Image Sci.*, 11, 1491–1499, 1994.

Evans, K. F., and G. L. Stephens, Microwave radiative transfer through clouds composed of realistically shaped ice crystals, part I, Single scattering properties, *J. Atmos. Sci.*, 52, 2041–2057, 1995.

Evans, K. F., S. J. Walter, A. J. Heymsfield, and M. N. Deeter, Modeling of submillimeter passive remote sensing of cirrus clouds, *J. Appl. Meteorol.*, 37, 184–205, 1998.

Evans, K. F., A. H. Evans, I. G. Nolt, and B. T. Marshall, The prospect for remote sensing of cirrus clouds with a submillimeter wave spectrometer, *J. Appl. Meteorol.*, 38, 514–525, 1999.

Foot, J. S., Some observations of the optical properties of clouds, II, Cirrus, *Q. J. R. Meteorol. Soc.*, 114, 145–164, 1988.

Francis, P. N., A. Jones, R. W. Saunders, K. P. Shine, A. Slingo, and Z. Sun, An observational and theoretical study of the radiative properties of cirrus: Some results from ICE'89, *Q. J. R. Meteorol. Soc.*, 120, 809–848, 1994.

Fu, Q., An accurate parameterization of the solar radiative properties of cirrus clouds for climate models, *J. Clim.*, 9, 2058–2082, 1996.

Fu, Q., P. Yang, and W. B. Sun, An accurate parameterization of the infrared radiative properties of cirrus clouds for climate models, *J. Clim.*, 25, 2223–2237, 1998.

Fu, Q., W. B. Sun, and P. Yang, On modeling of scattering and absorption by cirrus nonspherical ice particles at thermal infrared wavelengths, *J. Atmos. Sci.*, 56, 2937–2947, 1999.

Gao, B.-C., P. Yang, W. Han, R.-R. Li, and W. J. Wiscombe, An algorithm using visible and 1.38-µm channels to retrieve cirrus cloud reflectances from aircraft and satellite data, *IEEE Trans. Geosci. Remote Sens.*, 40, 1659–1668, 2002.

Grenfell, T. C., and S. G. Warren, Representation of nonspherical ice particle by a collection of independent sphere for scattering and absorption of radiation, *J. Geophys. Res.*, 104, 31,697–31,709, 1999.

Heidinger, A., Nadir sounding of clouds and aerosol in the O_2 A-band, *Atmos. Sci. Pap. 650*, Colo. State Univ., Fort Collins, Colo., 1998.

Heymsfield, A. J., S. Lewis, A. Bansemer, J. Iaquinta, L. M. Miloshevich, M. Kajikawa, C. Twohy, and M. R. Poellot, A general approach for deriving the properties of cirrus and stratiform ice cloud particles, *J. Atmos. Sci.*, 59, 3–29, 2002.

Kahn, B. H., A. Eldering, F. W. Irion, F. P. Mills, B. Sen, and M. R. Gunson, Cloud identification in atmospheric trace molecule spectroscopy infrared occultation measurements, *Appl. Opt.*, 41, 2768–2780, 2002.

Kratz, D. P., High resolution modeling of the far-infrared, *Proc. SPIE Int. Soc. Opt. Eng.*, 4485, 171–180, 2001.

Lee, Y. K., P. Yang, M. I. Mishchenko, B. A. Baum, Y. X. Hu, H.-L. Huang, W. J. Wiscombe, and A. J. Baran, Use of circular cylinders as surrogates for hexagonal pristine ice crystals in scattering calculations at infrared wavelengths, *Appl. Opt.*, 42, 2653–2664, 2003.

Liou, K. N., Influence of cirrus clouds on weather and climate processes: A global perspective, *Mon. Weather Rev.*, 114, 1167–1199, 1986.

Lynch, D. K., K. Sassen, D. O'C. Starr, and G. Stephens (Eds.), *Cirrus*, Oxford Univ. Press, New York, 2002.

Mannozzi, L., F. Di Giuseppe, and R. Rizzi, Cirrus cloud optical properties in the far infrared, *Phys. Chem. Earth*, 24, 269–273, 1999.

Mishchenko, M. I., and L. D. Travis, Capabilities and limitations of a current FORTRAN implementation of the T-matrix method for randomly oriented rotationally symmetric scatters, *J. Quant. Spectrosc. Radiat. Transfer*, 60, 309–324, 1998.

Mishchenko, M. I., J. W. Hovenier, and L. D. Travis (Eds.), *Light Scattering by Nonspherical Particles*, Academic, San Diego, Calif., 2000.

Mitchell, D. L., and W. P. Arnott, A model predicting the evolution of ice particle size spectra and radiative properties of cirrus clouds, part II, Dependence of absorption and extinction on ice crystal morphology, *J. Atmos. Sci.*, 51, 817–832, 1994.

Mitchell, D. L., A. Macke, and Y. Liu, Modeling cirrus clouds, II, Treatment of radiative properties, *J. Atmos. Sci.*, 53, 2967–2988, 1996.

Mlynczak, M. G., J. E. Harries, R. Rizzi, P. W. Stackhouse, D. P. Kratz, D. G. Johnson, C. J. Mertens, R. R. Garcia, and B. J. Soden, The far-infrared: A frontier in remote sensing of Earth's climate and energy balance, *Proc. SPIE Int. Soc. Opt. Eng.*, 4485, 150–158, 2002.

Purcell, E. M., and C. R. Pennypacker, Scattering and absorption of light by nonspherical dielectric grains, *Astrophys. J.*, 186, 705–714, 1973.

Rathke, C., J. Fischer, S. Neshyba, and M. Shupe, Improving IR cloud phase determination with 20 µm spectral observations, *Geophys. Res. Lett.*, 29, 501–504, 2002.

Rothman, L. S., et al., The HITRAN Molecular Spectroscopic Database and HAWKS (HITRAN Atmospheric Workstation): 1996 edition, *J. Quant. Spectrosc. Radiat. Transfer*, 60, 665–710, 1998.

Smith, W. L., X. L. Ma, S. A. Ackerman, H. E. Revercomb, and R. O. Knuteson, Remote sensing cloud properties from high-spectral resolution infrared observations, *J. Atmos. Sci.*, 50, 1708–1720, 1993.

Smith, W. L., S. Ackerman, H. Revercomb, H. Huang, D. H. DeSlover, W. Feltz, L. Gumley, and A. Collard, Infrared spectral absorption of nearly invisible cirrus clouds, *Geophys. Res. Lett.*, 25, 1137–1140, 1998.

Stamnes, K., S. C. Tsay, W. Wiscombe, and K. Jayaweera, A numerically stable algorithm for discrete-ordinate-method radiative transfer in multiple scattering and emitting layered media, *Appl. Opt.*, 27, 2502–2509, 1988.

Stephens, G. L., S. C. Tsay, P. W. Stackhouse, and P. J. Flatau, The relevance of the microphysical and radiative properties of cirrus clouds to climate and climate feedback, *J. Atmos. Sci.*, 47, 1742–1753, 1990.

Sun, W.-B., Q. Fu, and Z. Chen, Finite-difference time-domain solution of light scattering by dielectric particles with a perfectly matched layer absorbing boundary condition, *Appl. Opt.*, 38, 3141–3151, 1999.

Taflove, A., *Computational Electrodynamics: The Finite-Difference Time-Domain Method*, Artech House, Norwood, Mass., 1995.

Tobin, D. C., et al., Downwelling spectral radiance observations at the SHEBA ice station: Water vapor continuum measurements from 17–26 µm, *J. Geophys. Res.*, 104, 2081–2092, 1999.

Vanek, M. D., et al., Far-infrared sensor for cirrus (FITSC): An aircraft-based Fourier-transform spectrometer to measure cloud radiance, *Appl. Opt.*, 40, 2169–2176, 2001.

Warren, S. G., Optical constants of ice from the ultraviolet to the microwave, *Appl. Opt.*, 23, 1206–1225, 1984.

Yang, P., and K. N. Liou, Light scattering by hexagonal ice crystals: Comparison of finite-difference time domain and geometric optics methods, *J. Opt. Soc. Am. A. Opt. Image Sci.*, 12, 162–176, 1995.

Yang, P., and K. N. Liou, Finite-difference time domain method for light scattering by small ice crystals in three-dimensional space, *J. Opt. Soc. Am. A. Opt. Image Sci.*, 3, 2072–2085, 1996a.

Yang, P., and K. N. Liou, Geometric-optics-integral-equation method for light scattering by nonspherical ice crystals, *Appl. Opt.*, 35, 6568–6584, 1996b.

Yang, P., K. N. Liou, and W. P. Arnott, Extinction efficiency and single-scattering albedo of ice crystals in laboratory and natural cirrus clouds, *J. Geophys. Res.*, 102, 21,825–21,835, 1997.

Yang, P., B. C. Gao, B. A. Baum, Y. X. Hu, W. J. Wiscombe, S. C. Tsay, D. M. Winker, and S. L. Nasiri, Radiative properties of cirrus clouds in the infrared (8–13 µm) spectral region, *J. Quant. Spectrosc. Radiat. Transfer*, 70, 473–504, 2001.

————————

B. A. Baum, Y. X. Hu, D. P. Kratz, and M. G. Mlynczak, NASA Langley Research Center, MS 420, Hampton, VA 23681, USA.

A. Heidinger, Office of Research and Applications, National Environmental Satellite, Data, and Information Service, National Oceanic and Atmospheric Administration, Madison, WI 53706, USA.

M. I. Mishchenko, NASA Goddard Institute for Space Studies, New York, NY 10025, USA.

H. Wei and P. Yang, Department of Atmospheric Sciences, Texas A&M University, TAMU 3150, College Station, TX 77843-3150, USA. (pyang@ariel.met.tamu.edu)

W. J. Wiscombe, NASA Goddard Space Flight Center, Greenbelt, MD 20771, USA.